Terahertz response of patterned epitaxial graphene

Christian Sorger[1], Sascha Preu[1,2], Johannes Schmidt[3], Stephan Winnerl[3], Yuliy V. Bludov[4], Nuno M. R. Peres[4], Mikhail I. Vasilevskiy[4], Heiko B. Weber[1]

[1] Department of Physics, Friedrich-Alexander-University Erlangen-Nuremberg, Staudtstraße 7, 91058 Erlangen, Germany
[2] Department of Electrical Engineering and Information Technology, Technical University Darmstadt, Merckstraße 25, 64283 Darmstadt, Germany
[3] Institute of Ion Beam Physics and Materials Research, Helmholtz-Zentrum Dresden-Rossendorf, Bautzner Landstraße 400, 01314 Dresden, Germany
[4] Department of Physics and Center of Physics, University of Minho, Campus de Gualtar, P-4710-057 Braga, Portugal

E-mail: `heiko.weber@fau.de`

17 December 2015

Abstract. We study the interaction between polarized terahertz (THz) radiation and micro-structured large-area graphene in transmission geometry. In order to efficiently couple the radiation into the two-dimensional material, a lateral periodic patterning of a closed graphene sheet by intercalation doping into stripes is chosen. We observe unequal transmittance of the radiation polarized parallel and perpendicular to the stripes. The relative contrast, partly enhanced by Fabry-Perot oscillations reaches 20 %. The effect even increases up to 50 % when removing graphene stripes in analogy to a wire grid polarizer. The polarization dependence is analyzed in a large frequency range from < 80 GHz to 3 THz, including the plasmon-polariton resonance. The results are in excellent agreement with theoretical calculations based on the electronic energy spectrum of graphene and the electrodynamics of the patterned structure.

PACS numbers: 00.00, 20.00, 42.10

Keywords: Plasmonics, Graphene, THz, Grating

Submitted to: *New J. Phys.*

1. INTRODUCTION

Graphene's remarkable electrical and optical properties [1, 2, 3, 4] make it attractive for designing optoelectronic devices [5, 6]. Transparent in a broad optical frequency range, with a loss of only 2.3 % in the visible, graphene can be a good conductor under doping or electrostatic gating. The tunability of its conductivity, Fermi energy and, consequently, plasma oscillations offers a broad range of potential applications in the terahertz (THz) spectral range [1]. In this work, we demonstrate that patterned graphene can act as a grating, producing highly polarized THz radiation. The polarization effect is based on the coupling of the incident electromagnetic wave to surface plasmon-polaritons (SPPs) supported by doped graphene (for review see, e.g., Ref. [7, 5]).

We opt for epitaxial graphene because it can be grown continuously and homogeneously on large areas on a THz transparent highly resistive silicon carbide (SiC) substrate with epitaxial control, both as n-type [2] and p-type layers [8, 9]. Lithographic patterning allows for the formation of plasmonic gratings in order to enhance the interaction with light. The concept of gateless patterning [10] allows intercalation doping patterns within a closed graphene sheet, without a perturbing influence of metallic or electrolytic gates. We focus on patterns with a periodicity that is substantially smaller than the free-space THz wavelength (up to 3 orders of magnitude). Such plasmonic gratings are an important tool to manipulate light-matter interactions [1, 11], since they allow for the wave vector matching between the incident electromagnetic wave and SPPs. An additional advantage of the graphene/SiC system is that it allows for growing and even combining different graphene species in one sample, for instance, monolayer and quasi-freestanding bilayer graphene (QFBLG) [12]. In various materials, plasmonic enhancement has yet been utilized over more than three orders of magnitude in frequency, ranging from the near infrared (telecom band, 193 THz) [13, 14] down to the THz (100 GHz - 10 THz) range [15, 16].

The THz and infrared response of graphene has been investigated by Fourier transform infrared spectroscopy (FTIR). In contrast to our closed-sheet approach, the material has been cut into quasi-periodic pieces in order to generate pronounced plasmonic effects [17, 18, 19]. The samples include a rather complex stacking of wafer, dielectric, ionic liquid etc., such that the intrinsic response of graphene is not fully obvious. In particular, Fabry-Perot resonances which are expected in coplanar geometries are not resolved. The observed phenomena are particularly rich in the spectral vicinity of the SPP resonance. Simply spoken, below the SPP resonance frequency electrons can follow the electrical field, whereas they remain stationary above this frequency, associated with graphene's high transparency.

2. THEORETICAL BACKGROUND

As a first approximation to the problem, we note the plasma frequency of a continuous two-dimensional conductor [20] for a wavevector k

$$\omega_{\rm pl}^{(2D)}(k) = \sqrt{\frac{n^{(2{\rm D})}ke^2}{2m^*\epsilon_0\epsilon_{\rm r}}}, \tag{1}$$

where $n^{(2{\rm D})}$ is the charge density, e and ϵ_0 are the electron charge and the vacuum permittivity, $\epsilon_{\rm r}$ is the dielectric constant of the underlying medium and m^* denotes the effective mass. In the particular case of monolayer graphene $m^* = \hbar\sqrt{\pi n^{(2{\rm D})}}/v_{\rm F}$ (due to the Dirac-cone shape of charge-carrier spectrum), while for bilayer graphene case $m^* = t_\perp/(2v_{\rm F}^2)$, owing to the parabolic spectrum of electrons and holes. In this notation, $v_{\rm F}$ and $t_\perp$ are, respectively, the Fermi velocity and the interlayer coupling of bilayer graphene [21]. If graphene's conductivity is periodically modulated (in our case we use a stripe pattern with periodicity D), then the diffraction of the normally incident electromagnetic wave on periodicity results in the fact that the reflected and transmitted waves are constituted of an infinite series of spatial harmonics with in-plane vectors $k_l = 2\pi l/D$, where $l = (-\infty, \infty)$ is an integer. The SPP resonance frequency Ω_l (corresponding to l-th harmonics) is then estimated as

$$\Omega_l = \frac{4}{D}\sqrt{\frac{\alpha\pi lcdE_{\rm F}}{\hbar(\varepsilon_{\rm vac}+\varepsilon_{\rm SiC})}} = \omega_{\rm pl}^{(2{\rm D})}(k_l)\sqrt{\frac{d}{D}}, \tag{2}$$

where c is the velocity of light, α denotes the fine-structure constant, $\hbar$ is the Planck constant, $\varepsilon_{\rm vac}$ and $\varepsilon_{\rm SiC}$ are the dielectric constants of vacuum/air and the SiC-substrate, respectively. The plasma resonance is broadened by the momentum relaxation rate γ. We have developed a theory of the transmission near the SPP resonance employing a full electrodynamics simulation that is an adaption of our previous publication [22] to the present case (see section 1 in of the supplementary information available at `stacks.iop.org/njp/17/053045/mmedia`). It entirely takes into account the band structure of graphene and its specific characteristics (parametrized by the charge density n and the momentum relaxation rate γ), as well as the system geometry (period D and stripe width d) and the SiC substrate (thickness H and dielectric function $\varepsilon_{\rm SiC}$).

3. EXPERIMENTAL DETAILS

We use commercially available semi-insulating hexagonal SiC(0001) as a substrate for the subsequent growth of epitaxial graphene [2]. For periodic patterning we chose a minimum invasive technique that yields n-type and p-type epitaxial graphene side-by-side within a continuous graphene sheet by local intercalation which has been detailed in our previous publication [10]. For short, we exploit the inpenetrability of a closed MLG sheet for hydrogen atoms at intermediate temperatures, i.e. well below the intercalation temperature of MLG ($\approx 850\,^\circ$C [23]). We create artificial entry paths for the hydrogen by opening the graphene sheet locally. A regular array of voids (diameter ≈ 200 nm

and spacing 600 nm) is defined by standard electron beam lithography and oxygen plasma etching. Apart from these voids, the graphene sheet is still intact. Subsequent hydrogen treatment at 540 °C for 90 minutes leads to predefined hydrogen intercalation around the graphene voids. Here, we chose to define a stripe-like array of voids as sketched in Fig. 1(a). Microscopically, the hydrogen intercalation patterning chosen here affects also the interface layer (buffer layer [2]) in between MLG and its substrate SiC. Pristine, n-type MLG with charge carrier density $n \approx 10^{13}\,\mathrm{cm}^{-2}$ [displayed in blue in Fig. 1(a)] with buffer layer underneath (displayed in black) are merged with so-called QFBLG [8, 9] [displayed in red in Fig. 1(a), where the buffer layer has been converted into a second graphene sheet with $p \approx 10^{13}\,\mathrm{cm}^{-2}$]. Although the system forms a closed carbon bilayer sheet and differs only by a small amount of hydrogen, a materials contrast is introduced, as shown in scanning electron micrographs (SEM) in Figs. 1(b)-(d). Previous experiments have shown that the lateral contact between both graphene types behaves ohmic (i.e. linear IV characteristics) due to the absence of a band gap in graphene. It is certainly a nontrivial question whether this subtle modulation is capable of coupling the electrons in this two-dimensional graphene sheet to electromagnetic radiation. Using a scheme that has been developed in Ref. [10], we patterned large-area graphene into p- and n-type stripes to define plasmonic gratings, with a periodicity $D = 5\,\mu$m and QFBLG-width $d = 2.7\,\mu$m for sample PN1. In order to define a grating that comprises isolated MLG stripes, the as-grown material in between is removed by oxygen plasma etching. Full conversion of MLG- into the QFBLG-stripes is carried out by hydrogen treatment at 850 °C for 30 min.

The dependence of sample transmittance on frequency in the THz range was measured by using a continuous-wave (CW) as well as a pulsed THz time domain setup (TDS: Time Domain Spectroscopy). A n-i-pn-i-p superlattice photomixer is used as a THz source with tunable frequency for the CW measurements [24]. The polarized THz signal is focused onto the graphene:SiC sample using parabolic mirrors. The sample is mounted in the center of a rotation stage. While rotating the sample, the projection of the stripes onto the THz field is altered, resulting in an angle-dependent transmitted power, $P(\alpha)$, similar to a rotating wire grid polarizer. In particular, p-polarization and s-polarization can be selected, being defined as electric field components parallel or perpendicular to the periodicity of the grid, respectively [see Fig. 1(f)]. From the transmitted power, $P(\alpha)$, we extract the visibility V of p-polarized vs. s-polarized configuration,

$$V = \frac{P_\mathrm{p} - P_\mathrm{s}}{P_\mathrm{p} + P_\mathrm{s}} = \frac{T_\mathrm{p} - T_\mathrm{s}}{T_\mathrm{p} + T_\mathrm{s}} \tag{3}$$

where $T_\mathrm{i} = P_\mathrm{i}/P_\mathrm{ref}$ is the transmission coefficient, and P_ref is the transmission through the empty setup. V is a quantity that is reliably extracted from the measurement, as it compensates intensity drift and redundantizes reference spectra P_ref. A Golay cell detector is used for direct detection. Due to limited dynamic range at higher frequencies, CW data were only taken below 1 THz at ambient conditions.

TDS measurements were carried out in a dry nitrogen purged environment in order

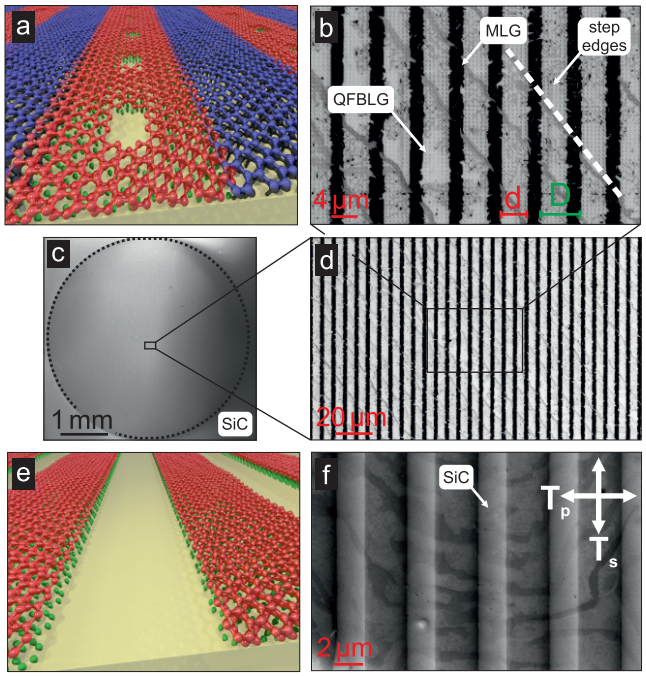

Figure 1. (a) Artist's view of a stripe pattern of intercalation-doping within the epitaxial graphene layer on SiC. The n-type MLG sheet is drawn in blue, with the buffer layer (black) underneath. Local insertion of hydrogen (green) through predefined voids results in p-type QFBLG (red). (b) - (d) Scanning electron micrographs depicting an alternating stripe pattern of QFBLG and MLG (similar to sample PN1). Substrate step edges are oriented in a different angle. (e) Artist's view of an array of isolated stripes of QFBLG (samples P1-P3). (f) Scanning electron micrograph of sample P1 depicting isolated stripes of QFBLG (light grey). In P1, step edges of the SiC are randomly oriented. Trilayer decoration is visible in SEM, but does not contribute to the experiment.

to extend the frequency range towards ≈ 3 THz. An 800 nm (Ti:Sapphire system, pulse duration 50 fs) driven large area emitter (LAE) [25] was used to generate highly polarized THz radiation. The transmitted THz-pulses were detected in the time domain by the electro-optic sampling method. The frequency spectrum is obtained by Fourier transformation of the main transmitted pulse only [single pass transmittivity, inset of Fig. 2(b), solid box] or including the first reflection [inset of Fig. 2(b), dashed box]. The latter is required for comparison with CW data in order to take into account Fabry-Perot (FP) features. The transmission setup was similar to the CW setup. All measurements were performed at room temperature.

4. EXPERIMENTAL RESULTS AND DISCUSSION

4.1. Continuous-Sheet Graphene with Intercalation Patterns

Fig. 2(a) displays the visibility as a function of the frequency of sample PN1. Obviously, the visibility is oscillatory due to FP-like multiple reflections at the front and back side of

the sample (wafer thickness $H = 490\,\mu$m, $\varepsilon_{\mathrm{SiC}} \approx 10$ [26], see inset). It oscillates between ≈ 0.01 and ≈ 0.12 corresponding to a polarization-dependent difference in transmission up to 20 %. The visibility in the maxima decreases with increasing frequency, which indicates the approximation to the SPP resonance. Note that higher order Fabry-Perot resonances, which arise due to the presence of the SiC substrate, increase the visibility in the maxima considerably. The single pass visibility that is extracted from TDS data relates to the patterned graphene sheet exclusively.

For getting closer to the resonance, we enhance the spectral region by employing TDS measurements. Single pass TDS and CW measurements for the same sample are shown in Fig. 2(a) without rescaling. The two different data sets match excellently. The visibility drops below zero, which indicates that T_{p} becomes smaller than T_{s}. At higher frequencies a minimum in the visibility indicates the SPP resonance at $f = 2.3 \pm 0.3\,$THz (strictly spoken, the resonance coincides with the minimum only in the limit of $\Omega_{\mathrm{l}} \gg \gamma$; as outlined in section 3.3 in the supplementary information). At this point, the THz radiation and the electron plasma are in resonance: T_{p} reaches its minimum (due to the fact, that SPP are p-polarized waves), whereas T_{s} is essentially unaffected. When further increasing the frequency, the visibility rises again and reaches zero at $f \approx 3\,$THz, as both transmission components become equal. Beyond this frequency, the sample becomes highly transparent. Whereas a perfect polarizer would have visibility equal to unity, this device reaches visibilities of $\approx 12\,\%$, which is remarkably high given the very subtle materials contrast of the closed two-layer carbon sheet.

4.2. Graphene Stripe Patterns

In order to enhance this effect, and to simplify the setup, we increased the materials contrast drastically by designing periodic graphene (QFBLG: samples P1-P3 and MLG: sample N2, N3) stripe patterns, separated by areas where the graphene was entirely removed by oxygen-plasma etching [cf. Fig. 1(f)]. This is even more similar to a wire grid polarizer, but with an atomically thin metal. The experimental data of the visibility for sample P1 are shown in Fig. 2(b), where a geometry ($D = 6\,\mu$m, $d = 3.5\,\mu$m) similar to PN1 was chosen. The CW results show essentially the same FP-like oscillations, which are limited to frequencies below 450 GHz due to experimental imperfections. As expected, the maximum visibility is significantly higher than for sample PN1. The geometric parameters as well as the charge density $p = 8.4 \cdot 10^{12}\,\mathrm{cm}^{-2}$ (from Hall-effect studies) are known for sample P1. Hence, the momentum relaxation rate is the only parameter that needs to be adapted for comparison with theory. For $\gamma = 20\,$meV, a perfect match in the given spectral region is achieved. As the experimental data of CW and TDS look quite different, it is instructive to consider not only the first recorded pulse (single pass), but also the second pulse that results from signals reflected back and forth at the substrate surfaces [inset of Fig. 2(b)]. The result after Fourier transformation is displayed in Fig. 2(b) as oscillating long-dashed line (denoted 'TDS, sp + fp1'). Thus, the inclusion of the second pulse re-establishes the FP oscillations that immediately

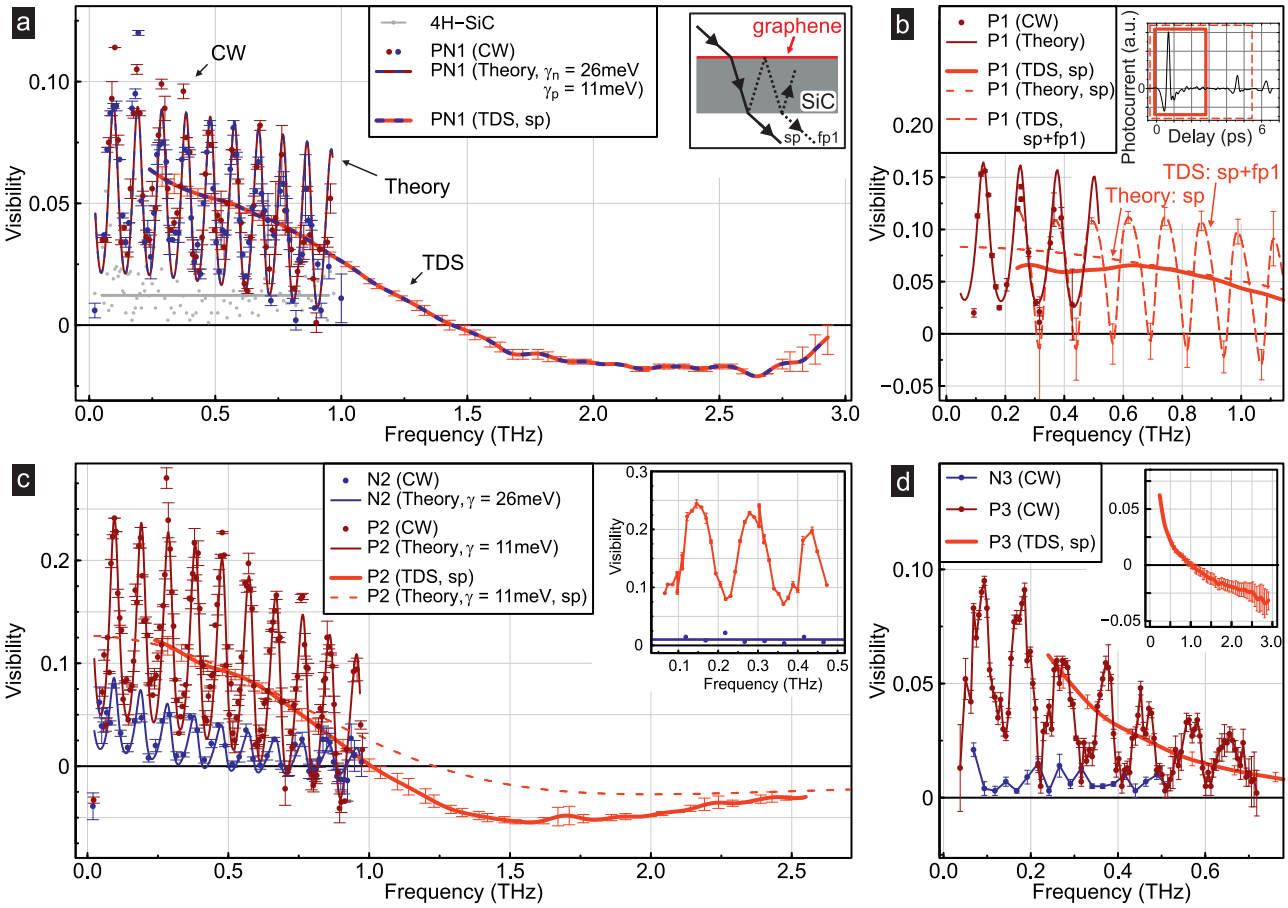

Figure 2. (a) Experimentally determined visibility of sample PN1 as a function of the excitation frequency as extracted from CW- (dark red symbols) and from TDS-measurements (thick line). Full electrodynamics simulation of the visibility (thinner line) coincides with the experimental CW data. No resolvable signal is recorded from the 4H-SiC substrate prior to graphene growth (grey symbols). In the inset the FP etalon is sketched. (b) Visibility of sample P1 as extracted from the CW- (dark red symbols) and the TDS-setup (solid and long-dashed red lines). Again, coincidence of CW data with theoretical calculations (dark red line) is obtained for $\gamma = 20\,\mathrm{meV}$. The inset shows the time-domain signal recorded in TDS-measurements, where the respective time windows have been indicated. (c) CW data for sample N2 (blue symbols) match the theoretical full wave simulation for single layer graphene (blue line). After intercalation, the resulting sample P2 (CW: dark red symbols; TDS: red line) displays a minimum at $f \approx 1.6\,\mathrm{THz}$. Coincidence with full wave simulation is achieved. Inset (control experiments): visibility signal from as-grown graphene samples (see text for details). (d) Experimental data for samples N3 (blue symbols) and P3 (CW: dark red symbols; TDS: red line). The inset shows the TDS data up to $f \approx 3\,\mathrm{THz}$. A minimum in the visibility is not observed within the measurement range.

connect to the CW data. Inclusion of even larger windows (i.e. higher order round trip pulses) in the time domain is not useful as experimental artefacts would then be included such as reflections within the detector crystal of the TDS system.

For an investigation of the resonance, we chose larger spatial periodicities of the stripe pattern (samples P2 and P3). Fig. 2(c) displays CW data of the visibility of sample P2 ($D = 20\,\mu$m, $d = 10\,\mu$m). The effect is qualitatively similar to P1, but with an increased amplitude in V at low frequencies – the difference in transmission reaches 50 % – and a significant decrease of the visibility towards 1 THz. The latter indicates the proximity to the resonance, which can be seen in the single pass TDS data of this sample, displayed in the same plot without rescaling. The two different data sets match excellently, and show a minimum of the visibility at $f \approx 1.6$ THz. Coincidence with full wave simulation is achieved for $\gamma = 11$ meV in the oscillatory region (dark red line). The dashed red line is the simulation in the single pass case. Visibility measurements of a third sample, P3, are displayed in Fig. 2(d). Due to the further increased length-scale of the stripe pattern ($D = 60\,\mu$m, $d = 30\,\mu$m), the SPP resonance is expected at a lower frequency $\Omega \approx 1$ THz. Similar to a mechanical oscillator, a higher momentum relaxation rate (relative to the resonance frequency) leads to a broadening of the resonance. Indeed, sample P3 can be considered as overdamped.

When carrying out the experiment with wire grid-like patterns, but using n-type MLG instead of p-type QFBLG, the data are very similar. The experiments were carried out on the very same samples, which are labeled N2 and N3 before intercalation, and P2 and P3 after intercalation, respectively. Figures 2(c) and 2(d) display the comparison of these data in a joint plot. It becomes obvious that the quasi-freestanding p-type material displays significantly larger visibilities. We assign this difference to the higher charge carrier mobility of the quasi-freestanding bilayer graphene at room temperature [9, 27]. The ratio of the momentum relaxation rates (26 meV / 11 meV = 2.36) agrees with the respective ratio obtained from the DC Hall mobilities for single layer graphene [9, 28].

4.3. Other Quasi-Periodic Patterns

It should be emphasized that other quasi-periodic patterns exist on any macroscopic SiC chip due to step edges of the SiC substrate. They may be randomly oriented (approximately on-axis wafer cut, with a flower-like step edge pattern) or quasi-periodic due to intentional wafer miscut. We now quantify their influence. First, we investigate a SiC chip without any graphene. The CW measurement results in no resolvable visibility [cf. Fig. 2(a)]. In a next step, graphene is grown by thermal decomposition. In addition to the substrate steps, additional layer growth along the step edges is observed, which results in a quasi-periodic pattern. Depending on the homogeneity of the graphene layer on samples with aligned step edges the measured visibility varies significantly. The findings range from no resolvable visibility for a homogeneous coverage with graphene [inset in Fig. 2(c): blue symbols] up to a visibility of 25 % for aligned, 2 - 3 μm spaced

step edges decorated with a multitude of graphene flavors (red symbols). From SEM analysis we know that the graphene layer for the samples P2/P3 and N2/N3 was grown very homogeneously (little step edge decoration). As this periodicity can be rotated by a defined angle with respect to the lithographically induced pattern, its effect can be singled out by regarding the full angular dependence of the transmission. Further, we characterized samples, which have no quasi-periodic substrate-patterns but rather spatially randomized step-edges overgrown with graphene (on-axis sample). These samples show no detectable visibility. All these experiments confirm that the effect reported above on samples P1 - P3 and N2 - N3 is due to the lithographically defined pattern and only to a minor extent due to quasi-periodic sample features. The case is more complicated for the PN sample, as the fabrication process for the periodic intercalation stripe pattern creates a periodic array of voids [cf. Fig. 1(b)]. We quantified the effect of the void array on the visibility prior to intercalation, i.e. in a homogeneous n-type graphene sheet. It turns out that the signal induced by the void pattern is negligible.

4.4. Theoretical Description of Intercalation Patterned Graphene

The details of our theoretical model are presented in section 1 and 2 in the supplementary information, including the description of the scattering problem using a transfer matrix formalism, and the derivation of the optical conductivity for bilayer graphene. The calculations yield reflectance and transmittance spectra for two polarizations of the incident radiation (an example is shown in Fig. 3), from which the theoretical visibility spectra presented in Fig. 2 for samples P1, P2 and N2 were obtained. It is clear, that the coupling of the p-polarized incident electromagnetic wave to surface plasmons yields a pronounced minimum of the transmittance (left panel in Fig. 3), while there is no such a coupling for s-polarized waves (right panel in Fig. 3). A discussion of the SPP resonances that determine the difference between the p- and s-polarized spectra can also be found in section 1 in supplementary information.

After having demonstrated that samples P1 - P3 and N2 behave like a wire-grid polarizer (with insulating regions in between) and can qualitatively and quantitatively be described by the full wave simulation, we return to the PN sample. It is different, because it provides only one closed conducting sheet composed of two different materials. For the simulation we assumed a stripe-like periodic pattern of alternating n- and p-doped regions and employed the momentum relaxation rates ($\gamma_\mathrm{p} = 11\,\mathrm{meV}$, $\gamma_\mathrm{n} = 26\,\mathrm{meV}$) derived from P2 and N2 as input parameters for the calculation. The result is displayed in Fig. 2(a) as solid oscillating line, together with the experimental data already discussed above. We achieve an excellent match with the CW data. This finding implies that the p-n junction in graphene (having no band gap) has little relevance to the observed phenomena. The response of the structure is determined by the conductivity contrast within the structure's period.

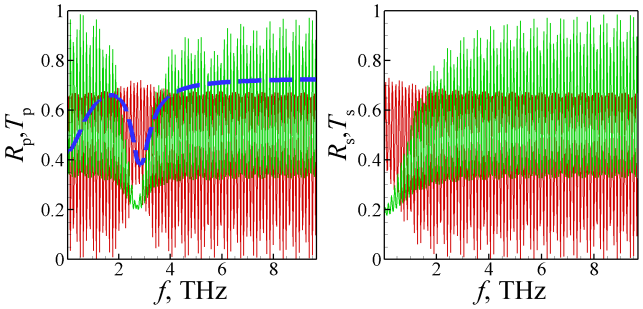

Figure 3. Calculated reflectance (red lines) and transmittance (green line) versus frequency ω for array of bilayer graphene stripes with parameters $p = 8.4 \cdot 10^{12}\,\mathrm{cm}^{-2}$, $\gamma = 2.6\,\mathrm{meV}$, $d = 3.5\,\mu\mathrm{m}$, $D = 6\,\mu\mathrm{m}$, deposited on top of SiC substrate ($\varepsilon_{\mathrm{SiC}} = 10$) with thickness $H = 375\,\mu\mathrm{m}$ and surrounded by vacuum/air with $\varepsilon_{\mathrm{vac}} = 1$. Left and right panels correspond to p- and s-polarizations, respectively In left panel dashed blue line corresponds to the transmission, obtained from the three-harmonic approximation (equation (5) in the supplementary information) for the same parameters.

5. CONCLUSIONS

We have demonstrated several possibilities to control the THz transmission through an epitaxial graphene layer by purposeful, periodic patterning. It is remarkable that graphene, despite it is atomically thin and almost fully transparent in the visible, can reduce the transmission by 50 % when stripes are patterned in analogy to a wire grid polarizer in the case of epitaxial graphene. When employing only a very subtle materials contrast by periodic intercalation of hydrogen, even a graphene sheet that covers the full area can reach a reduction of transmission as large as 20 %. We achieve excellent, qualitative and quantitative agreement with theory based on the electronic energy spectrum of the graphene and electrodynamics of the periodically patterned structure. By appropriate design of the periodic pattern, the transition from a metallic DC behavior to the optical regime can be studied in the THz regime, giving access to the plasmon-polariton resonance.

Acknowledgments

The authors thank J. Jobst for fruitful discussions. The research was performed in the framework of the Sonderforschungsbereich 953 "Synthetic carbon allotropes", funded by Deutsche Forschungsgemeinschaft. We acknowledge support from the EC under Graphene Flagship (contract no. CNECT-ICT-604391).

References

[1] A. N. Grigorenko, M. Polini, and K. S. Novoselov. Graphene plasmonics. *Nature Photonics*, 6:749–758, 2012.

[2] K. V. Emtsev, A. Bostwick, K. Horn, J. Jobst, G. L. Kellogg, L. Ley, J. L. McChesney, T. Ohta, S. A. Reshanov, J. Röhrl, E. Rotenberg, A. K. Schmid, D. Waldmann, H. B. Weber, and

T. Seyller. Towards wafer-size graphene layers by atmospheric pressure graphitization of silicon carbide. *Nature Mater.*, 8:203, 2009.

[3] A. H. Castro Neto, F. Guinea, N. M. R. Peres, K. S. Novoselov, and A. K. Geim. The electronic properties of graphene. *Rev. Mod. Phys.*, 81:109–162, Jan 2009.

[4] Aires Ferreira, J. Viana-Gomes, Johan Nilsson, E. R. Mucciolo, N. M. R. Peres, and A. H. Castro Neto. Unified description of the dc conductivity of monolayer and bilayer graphene at finite densities based on resonant scatterers. *Phys. Rev. B*, 83:165402, Apr 2011.

[5] M. Jablan, M. Soljacic, and H. Buljan. Plasmons in graphene: Fundamental properties and potential applications. *Proceedings of the IEEE*, 101(7):1689–1704, July 2013.

[6] F Bonaccorso, Z Sun, T Hasan, and A C Ferrari. Graphene photonics and optoelectronics. *Nature Photonics*, 4(9):611–622, sep 2010.

[7] Tobias Stauber. Plasmonics in dirac systems: from graphene to topological insulators. *Journal of Physics: Condensed Matter*, 26(12):123201, 2014.

[8] C. Riedl, C. Coletti, T. Iwasaki, A. A. Zakharov, and U. Starke. Quasi-Free-Standing Epitaxial Graphene on SiC Obtained by Hydrogen Intercalation. *Phys. Rev. Lett.*, 103:246804, 2009.

[9] F. Speck, J. Jobst, F. Fromm, M. Ostler, D. Waldmann, M. Hundhausen, H. B. Weber, and T. Seyller. The Quasi-Free-Standing Nature of Graphene on H-Saturated SiC (0001). *Appl. Phys. Lett.*, 99:122106–122106, 2011.

[10] C. Sorger, S. Hertel, J. Jobst, C. Steiner, K. Meil, K. Ullmann, A. Albert, Y. Wang, M. Krieger, J. Ristein, S. Maier, and H. B. Weber. Gateless patterning of epitaxial graphene by local intercalation. *Nanotechnology*, 26:025302, 2015.

[11] J. A. Schuller, E. S. Barnard, W. Cai, Y. C. Jun, J. S. Whiteand, and M. L. Brongersma. Plasmonics for Extreme Light Concentration and Manipulation. *Nature Mater.*, 9:193, 2010.

[12] S. Hertel, D. Waldmann, J. Jobst, A. Albert, M. Albrecht, S. Reshanov, A. Schöner, M. Krieger, and H. B. Weber. Tailoring the graphene/silicon carbide interface for monolithic wafer-scale electronics. *Nature Commun.*, 3:957:1, 2012.

[13] J. Wen, S. Romanov, and U. Peschel. Excitation of Plasmonic Gap Waveguides by Nanoantennas. *Opt. Express*, 17:5925–5932, 2009.

[14] A. Kriesch, S. O. Burgos, D. Ploss, H. Pfeifer, H. A. Atwaterand, and U. Peschel. Functional Plasmonic Nanocircuits with Low Insertion and Propagation Losses. *Nano Lett.*, 13:4539–4545, 2013.

[15] I. Crassee, M. Orlita, M. Potemski, A. L. Walter, M. Ostler, T. Seyller, I. Gaponenko, J. Chen, and A. B. Kuzmenko. Intrinsic Terahertz Plasmons and Magnetoplasmons in Large Scale Monolayer Graphene. *Nano Lett.*, 12:2470–2474, 2012.

[16] C. W. Berry, N. Wang, M. R. Hashemi, M. Unlu, and M. Jarrahi. Significant Performance Enhancement in Photoconductive Terahertz Optoelectronics by Incorporating Plasmonic Contact Electrodes. *Nature Commun.*, 4:1622, 2013.

[17] L. Ju, B. Geng, J. Horng, C. Girit, M. Martin, Z. Hao, H. A Bechtel, X. Liang, A. Zettl, Y. R. Shen, and F. Wang. Graphene Plasmonics for Tunable Terahertz Metamaterials. *Nature Nanotechnol.*, 6:630–634, 2011.

[18] Hugen Yan, Xuesong Li, Bhupesh Chandra, George Tulevski, Yanqing Wu, Marcus Freitag, Wenjuan Zhu, Phaedon Avouris, and Fengnian Xia. Tunable infrared plasmonic devices using graphene/insulator stacks. *Nature Nanotechnol.*, 7(5):330–334, 2012.

[19] Hugen Yan, Tony Low, Wenjuan Zhu, Yanqing Wu, Marcus Freitag, Xuesong Li, Francisco Guinea, Phaedon Avouris, and Fengnian Xia. Damping pathways of mid-infrared plasmons in graphene nanostructures. *Nature Photonics*, 7(5):394–399, 2013.

[20] G. C. Dyer, J. D. Crossno, G. R. Aizin, E. A. Shaner, M. C. Wanke, J. L. Reno, and S. J. Allen. A Plasmonic Terahertz Detector with a Monolithic Hot Electron Bolometer. *J. Phys.-Condens. Matt.*, 21:195803, 2009.

[21] E. McCann and M. Koshino. The Electronic Properties of Bilayer Graphene. *Rep. Prog. Phys.*, 76:056503, 2013.

[22] Y. V. Bludov, A. Ferreira, N. M. R. Peres, and M. I. Vasilevskiy. A Primer on Surface Plasmon-Polaritons in Graphene. *International Journal of Modern Physics B*, 27(10):1341001, 2013.

[23] Samir Mammadov, Jrgen Ristein, Roland J Koch, Markus Ostler, Christian Raidel, Martina Wanke, Remigijus Vasiliauskas, Rositza Yakimova, and Thomas Seyller. Polarization doping of graphene on silicon carbide. *2D Materials*, 1(3):035003, 2014.

[24] S. Preu, G. Döhler, S. Malzer, L. J. Wang, and A. C. Gossard. Tunable, continuous-wave Terahertz photomixer sources and applications. *J. Appl. Phys.*, 109:061301, 2011.

[25] S. Winnerl. Scalable Microstructured Photoconductive Terahertz Emitters. *J. Infrared. Millim. Thz Waves*, 33:431–454, 2012.

[26] Lyle Patrick and WJ Choyke. Static dielectric constant of sic. *Phys. Rev. B*, 2:2255–2256, 1970.

[27] Joshua A Robinson, Matthew Hollander, Michael LaBella III, Kathleen A Trumbull, Randall Cavalero, and David W Snyder. Epitaxial graphene transistors: enhancing performance via hydrogen intercalation. *Nano Lett.*, 11(9):3875–3880, 2011.

[28] J. Jobst, D. Waldmann, F. Speck, R. Hirner, D. K. Maude, T. Seyller, and H. B. Weber. Quantum oscillations and quantum Hall effect in epitaxial graphene. *Phys. Rev. B*, 81:195434, 2010.